Manganese Oxide as a Promoter for Copper Catalysts in CO$_2$ and CO Hydrogenation

Remco Dalebout[+],[a] Laura Barberis[+],[a] Nienke L. Visser,[a] Jessi E. S. van der Hoeven,[a] Ad M. J. van der Eerden,[a] Joseph A. Stewart,[b] Florian Meirer,[c] Krijn P. de Jong,[a] and Petra E. de Jongh*[a]

In this work, we discuss the role of manganese oxide as a promoter in Cu catalysts supported on graphitic carbon during hydrogenation of CO$_2$ and CO. MnO$_x$ is a selectivity modifier in an H$_2$/CO$_2$ feed and is a highly effective activity promoter in an H$_2$/CO feed. Interestingly, the presence of MnO$_x$ suppresses the methanol formation from CO$_2$ (TOF of $0.7 \cdot 10^{-3}$ s^{-1} at 533 K and 40 bar) and enhances the low-temperature reverse water-gas shift reaction (TOF of $5.7 \cdot 10^{-3}$ s^{-1}) with a selectivity to CO of 87%$_C$. Using time-resolved XAS at high temperatures and pressures, we find significant absorption of CO$_2$ to the MnO, which is reversed if CO$_2$ is removed from the feed. This work reveals fundamental differences in the promoting effect of MnO$_x$ and ZnO$_x$ and contributes to a better understanding of the role of reducible oxide promoters in Cu-based hydrogenation catalysts.

Introduction

Promoters are found in many supported catalysts.[1,2] They are generally present in low concentrations and, while usually being catalytically inactive for a specific reaction, they substantially boost catalyst activity, selectivity, and/or stability.[3] For instance, in methanol production from CO$_2$-enriched syngas (H$_2$/CO) the addition of a ZnO$_x$ promoter to the Cu/Al$_2$O$_3$ system leads to an activity enhancement of an order of magnitude.[4–6] This activity increase has made the Cu/ZnO/Al$_2$O$_3$ catalyst the established industrial catalyst for the synthesis of methanol from syngas since the 1960s.[7] Another interesting feature of this reaction is that it has been shown that it is the CO$_2$ in the feed that is converted into methanol,[6,8–10] and hence this system can form an important starting point for Cu-catalyzed pure CO$_2$ hydrogenation.

Elucidating the change in catalyst properties induced by various feed compositions is of significant importance. The rising CO$_2$ concentration in the atmosphere has pushed the interest in research to convert CO$_2$ in large industrial processes such as methanol synthesis from syngas. Yet, catalysts for use in a feed purely based on CO$_2$ and H$_2$ face challenges. For example, without CO in the feed Cu/ZnO/Al$_2$O$_3$ catalysts face faster thermal growth of the Cu particles and a significantly lower methanol selectivity.[11] The Cu particle growth is accelerated by the extra water formed during CO$_2$ hydrogenation to either methanol [Eq. (1)] or CO (the reverse water-gas shift (RWGS) reaction, [Eq. (2)]). CO$_2$ hydrogenation to methanol is an exothermic reaction but entropically very unfavorable, hence high pressures are needed to reach reasonable equilibrium conversion (e.g. 26.2%$_C$ methanol at 40 bar and 473 K with an H$_2$/CO$_2$ ratio of 3). On the other hand, the RWGS reaction is endothermic and entropically slightly favorable. It is hence expected that control over the experimental conditions such as pressure, temperature, and gas composition is key to selectively obtain the desired product. Additionally, promoters can play a key role in product selectivity.

	$\Delta_r H^{\ominus}$ (kJ mol^{-1})	$\Delta_r S^{\ominus}$ (J mol^{-1} K^{-1})	$\Delta_r G^{\ominus}$ (kJ mol^{-1})	
CO$_2$ + 3H$_2$ ⇌ CH$_3$OH + H$_2$O	−49.3	−177	+3.48	(1)
CO$_2$ + H$_2$ ⇌ CO + H$_2$O	+41.1	+42.0	+28.6	(2)

Reducible metal oxides are particularly effective promoters in gas-phase hydrogenation reactions. Their rich chemistry is based on the changes in the oxidation state of the metal, facile and reversible creation of oxygen vacancies, and metal–metal interactions of the oxide.[12–16] Starting from a high oxidation state, reduction to a lower metal oxidation state forms an

[a] R. Dalebout,[+] L. Barberis,[+] N. L. Visser, Dr. J. E. S. van der Hoeven, A. M. J. van der Eerden, Prof. K. P. de Jong, Prof. P. E. de Jongh
Materials Chemistry and Catalysis
Debye Institute for Nanomaterials Science
Utrecht University
Universiteitsweg 99
3584 CG, Utrecht (The Netherlands)
E-mail: P.E.deJongh@uu.nl

[b] Dr. J. A. Stewart
TotalEnergies OneTech Belgium
Zone industrielle C
B-7181 Seneffe (Belgium)

[c] F. Meirer
Inorganic Chemistry and Catalysis
Debye Institute for Nanomaterials Science
Utrecht University
Universiteitsweg 99
3584 CG, Utrecht (The Netherlands)

[+] Authors contributed equally to this work.

ChemCatChem

Research Article
doi.org/10.1002/cctc.202200451

**Chemistry
Europe**
European Chemical
Societies Publishing

oxygen vacancy. In turn, this results in an excess of electrons, which is redistributed to the cation empty energy level causing a change in the oxidation state of the cation M^{n+} to $M^{(n-1)+}$. For this reason, metals that contain half-filled d and f orbitals, and hence have a variety of stable oxidation states, typically are redox active.[17,18] The presence of electropositive sites (vacancies) can have important effects during catalysis, particularly influencing the adsorption properties of reactants and intermediate species, e.g. favoring CO_2 adsorption and activation due to its electrophilic character.[19–21] Improvements in catalytic performance in methanol synthesis resulting from the use of reducible oxides as promoters in Cu-based catalysts have been reported for many reducible oxides, with ZnO_x being the most recurrent, but the nature of the metal–metal oxide interaction has been far from fully understood.[13,22–25]

MnO_x is an interesting oxide as Mn has a rich variety of metal oxidation states ($+2, +3, +4, +5, +6, +7$), low cost, and high abundancy. Despite this, only limited literature is available regarding the use of MnO_x as a promoter in hydrogenation reactions, specifically for Cu-catalyzed CO_2 and/or CO hydrogenation. MnO_x has been reported to boost the total activity, either attributed to changing the size and dispersion of the Cu nanoparticles,[20,23,26–28] to electronic promotion due to a specific Cu–MnO_x synergy,[27–29] or to its influence on the concentration of basic surface sites that increase the CO_2 dissociation activity.[28,30] As an example of electronic promotion, for NO reduction by CO the formation of oxygen vacancies in $(CuMn)_3O_4$, specifically $Cu^{(y-1)+}$-□-$Mn^{(x-1)+}$, is reported to be the main active site for N_2 production as proven by in situ spectroscopy and DFT calculations.[21] MnO_x is also reported to increase the methanol selectivity during high-pressure hydrogenation of a CO_2-rich syngas feed, which is proposed to be due to the presence of surface Cu^+ species[26,31] or stabilization of specific reaction intermediates.[20] There are also hints that MnO_x might increase the thermal stability of Cu nanoparticles,[28] but its effect appears to be less pronounced than for a ZnO_x promoter[32,33] and mechanistic details remain unclear. There are still many open questions as other reports suggest the absence of any electronic promotion of Cu nanoparticles by MnO_x[34] or that not the selectivity to methanol but to CO increased upon MnO_x addition.[32]

The complexity of supported catalysts, e.g. partial mixing the oxidic promoter and oxidic support, has partly been responsible for the limited understanding of the role of reducible oxides in catalysis.[35,36] Recently, we reported that a silica support for ZnO_x-promoted Cu nanoparticles plays a significant role in reducing the efficacy of the ZnO_x promoter due to the formation of a large fraction of inactive Zn spectator species bound to the silica.[37] The use of an inert support such as graphitic carbon allows reducing this complexity and enables a more targeted investigation of structure, properties, and catalytic functioning of reducible oxide-promoted catalysts.

Another reason why the promotion of Cu nanoparticles by reducible oxides is far from fully understood is the dynamic nature of the catalysts under working (high-pressure) conditions[38] and hence the need for operando studies. In situ X-ray absorption spectroscopy (XAS) is a powerful technique

with the ability to elucidate the nature of metal–Oxide species under reaction conditions.[39–44] In this work, operando XAS is employed as a tool to study the dynamic changes in Cu and Mn interaction by following the oxidation state, electronic structure, and local bonding environment during in situ reduction and high temperature and pressure CO_2 and/or CO hydrogenation to methanol. We combine this with results on the impact of MnO_x on the activity, selectivity, and stability of the Cu-catalyzed hydrogenation of CO and CO_2, and highlight the fundamental difference in the promoting effect between MnO_x and ZnO_x.

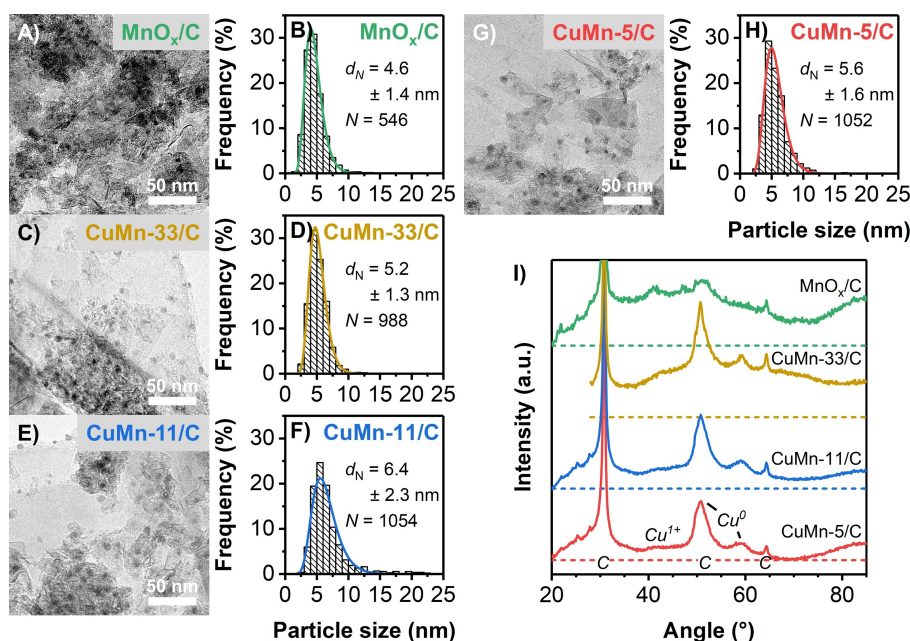## Results

Structural Properties of the Catalysts

A main challenge in studying the influence of a promoter is to vary the promoter content while keeping all other variables constant, such as the size of the metal nanoparticles.[45,46] Figure 1 (frames A–H) shows electron micrographs of selected $CuMnO_x$/C catalysts with the corresponding particle size distributions. The full overview of representative electron micrographs and particle size distributions of each catalyst is given in Figure S1, and the surface-averaged particle sizes are summarized in Table 1. All Cu(Mn)O_x/C catalysts had a Cu loading of ca. 8.5 wt%, but their Mn/(Cu+Mn) molar content ranged from 0 to 33 at%, as indicated in the sample name. For example, the CuMn-11/C catalyst contained 11 at% MnO_x. In all cases a good spatial distribution of the CuO_x nanoparticles (black dots) over the sheet-like carbon support (light grey) was obtained. The average particles sizes were between 5 and 7 nm, irrespective of the MnO_x loading (Table 1). The Cu/C catalyst had slightly larger particles (10 nm) as it is challenging to synthesize small CuO_x particles supported on carbon without any additives.[47] MnO_x is thus also a structural promoter in Cu/C catalysts by enhancing or stabilizing a smaller Cu particle size. An MnO_x/C catalyst with 7.2 wt% Mn was prepared as a reference. The catalyst synthesis[46] was reproducible as shown by three batches of the CuMn-20/C catalyst, which had surface-average particle sizes of 5.5 ± 1.9 nm, 5.7 ± 1.6 nm, and 5.1 ± 1.7 nm, respectively (Figure S2).

The presence of crystalline phases was detected by X-ray powder diffraction (XRD), both after catalyst synthesis in the reduced state and after passivation. The diffractograms of

Table 1. Surface-averaged $CuMnO_x$ particle diameters (in nm) of $CuMnO_x$/C catalysts in the fresh and used state determined by TEM. The particles were passivated prior to the measurement. Details are given in Table S1.

catalyst	fresh	used
Cu/C	9.9 ± 3.3	11.6 ± 4.4 [a]
CuMn-5/C	5.8 ± 1.6	6.3 ± 1.8
CuMn-11/C	6.9 ± 2.3	6.5 ± 2.0
CuMn-20/C	5.5 ± 1.9	6.7 ± 2.4
CuMn-33/C	5.4 ± 1.3	6.6 ± 2.1
MnO_x/C	4.8 ± 1.4	9.3 ± 4.0
[a] After 160 h of catalysis.		

ChemCatChem

Research Article
doi.org/10.1002/cctc.202200451

Chemistry
Europe
European Chemical
Societies Publishing

Figure 1. (**A,C,E,G**) TEM images and (**B,D,F,H**) corresponding particle size distributions of the MnO_x/C, CuMn-33/C, CuMn-11/C, and CuMn-5/C catalysts, respectively. (**I**) XRD patterns of selected $CuMnO_x/C$ catalysts in the reduced state; vertically offset for clarity.

selected reduced catalysts are shown in Figure 1 (frame I), while the patterns of the passivated catalysts are shown in Figure S3. After catalyst preparation, during which temperatures up to 673 K were used, the crystallinity of the carbon support was preserved, as demonstrated by the *(002)* diffraction line of graphite at 30.9°. The peaks at 50.9° and 59.5° for the CuMn-5/C and CuMn-11/C catalysts correspond to metallic Cu crystallites with an average size of only 3-4 nm, whereas for the CuMn-33/C catalyst the peaks are attributed to Cu^0 crystallites with a size of *ca.* 7-8 nm. Additional details on the crystallite sizes are given in Table S2. Specifically focusing on MnO_x, no crystalline Mn phases were detected in any of the catalysts. The amorphous background of the diffractograms increased when more MnO_x was present in the catalyst, which suggests that the MnO_x promoter was highly dispersed and/or amorphous. Energy-dispersive X-ray spectroscopy (EDX) maps shown in Figure 2 confirmed the presence of highly dispersed MnO_x over the graphitic support in coexistence with distinct MnO_x nanoparticles near the CuO_x nanoparticles. High-resolution scanning-transmission electron micrographs on a single Cu particle (Figure 2, frame C) showed a crystalline Cu structure surrounded by amorphous Mn particles, in agreement with XRD analysis.
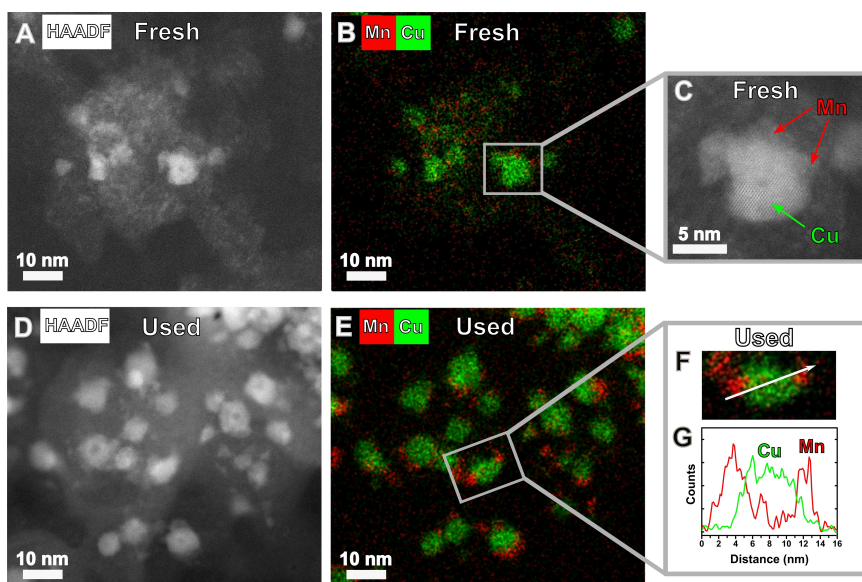
Interaction between Cu and MnO_x

We investigated the interaction of MnO_x with Cu in our carbon-supported samples by *ex situ* reduction by H_2 as well as *in situ*, time-resolved X-ray absorption spectroscopy (XAS). Figure 3 (frame A) shows the *ex situ* reduction profiles of selected catalysts (the complete overview is given in Figure S4). Note that probably all carbon surface groups were already reduced

before this measurement,[47–49] as the catalysts were H_2-treated at 673 K during catalyst synthesis. The Cu-free MnO_x species were (partially) reduced around 587 K, as indicated by the arrow. The reduction profiles changed significantly with the addition of Cu: a double peak around 433 K was observed, corresponding to the reduction of CuO via Cu^+ to Cu^0,[50,51] while the high-temperature reduction of MnO_x became much less pronounced. Furthermore, the offsets of the reduction peaks around 433 K were slightly higher for the CuMn-33/C (407 K) than for the CuMn-11/C catalyst (396 K). The increase in the reduction temperature at higher MnO_x loadings is a general trend observed across all $CuMnO_x/C$ catalysts (Table S3). Hence, from the *ex situ* reduction profiles it appears that Cu influences the reduction of MnO_x, indicating close contact between Cu and MnO_x, but *in situ* XAS is needed to study in more detail what happens.

Figure 3 (frames B–F) shows the evolution of the oxidation states of the Cu and Mn species during *in situ* H_2 treatment. The oxidation states were obtained by fitting linear combinations (LCF analysis) of the macrocrystalline references to the time-resolved XAS measurements depicted in Figures S10–S11. In all Cu-based catalysts (frames C–D) the CuO clearly was reduced in a two-step process to Cu^0 *via* the formation of Cu^+, which is a typical two-step conversion also reported in literature[50,52] and which explains the double peak observed around 433 K in frames A. Furthermore, the Cu species in the CuMn-11/C catalyst had an oxidation state slightly below +2 (+1.90, frame C), while the CuMn-33/C catalyst contained fully oxidized CuO (frame D). The CuO reduction was not significantly affected by the presence of MnO_x.

Focusing on the Mn species, in the absence of Cu the MnO_x was slowly reduced from Mn_2O_3 to mainly MnO upon holding

ChemCatChem

Research Article
doi.org/10.1002/cctc.202200451

Chemistry
Europe

European Chemical
Societies Publishing

Figure 2. HAADF-STEM-EDX analysis for the passivated CuMn-33/C catalyst in the fresh and used state. (**A,D**) Scanning-transmission electron microscopy (STEM) images using a high-angle, annular, dark field (HAADF) detector. (**B,E**) Energy-dispersive X-ray spectroscopy (EDX) maps showing the elemental distributions for Cu (green) and Mn (red). (**C**) High-resolution zoom (grey square) of a highly crystalline Cu nanoparticle in close contact with amorphous Mn. (**G**) Line scan of the EDX map taken over the length of the indicated region (**F**).
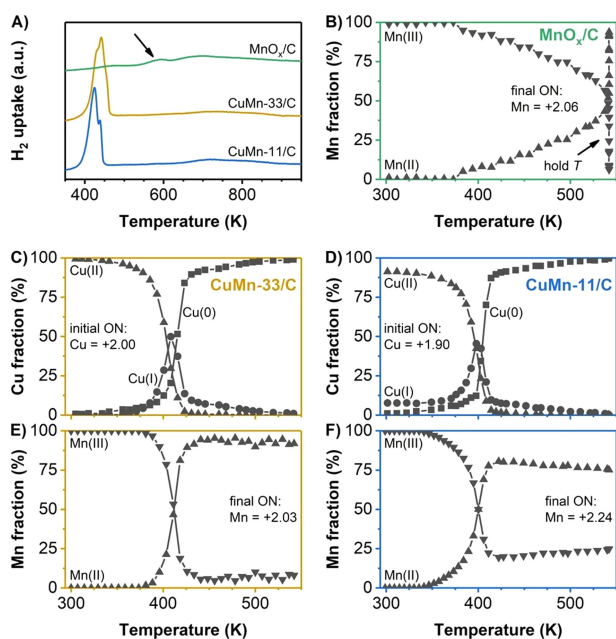
Figure 3. (**A**) Reduction profiles of selected $CuMnO_x/C$ catalysts, which are vertically offset for clarity and normalized by the support amount (50 mg catalyst). The arrow indicates the (partial) reduction of MnO_x species. Conditions: dried at 393 K in Ar, TPR with 5 vol % H_2/Ar, ramp 2.5 K min^{-1}, 0.5 L min^{-1} g^{-1}. (**B–F**) Results from linear combination fitting (LCF) of the Cu and Mn oxidation states of the CuMn-11/C, CuMn-33/C, and MnO_x/C catalysts, derived from time-resolved XAS measurements and using the references displayed in Figures S10-S11. Conditions: 20 vol % H_2/He, ramp 2.5 K min^{-1}, ca. 2.5–3.3 L min^{-1} g^{-1}. ON = oxidation number.

catalysts (frames E–F) was reduced at a much lower temperature around 405 K and exactly at the same temperature as CuO. The combined reduction proceeded at a slightly lower temperature in the CuMn-11/C catalyst (400 K) than in the CuMn-33/C catalyst (410 K), in line with the *ex situ* reduction by H_2 (frame A). Hence, with *in situ* XAS we showed that (virtually) all MnO_x was influenced by the close vicinity of Cu and that Cu induced the reduction of Mn_2O_3 at a very low temperature as soon as metallic Cu was formed.
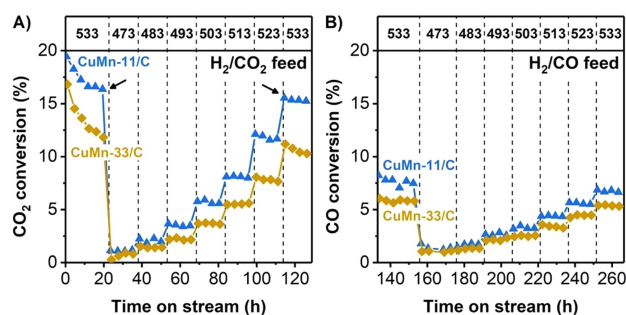
The MnO_x species consisted of (amorphous) Mn_2O_3 in the initial state, whereas upon heating in an H_2 atmosphere the Mn oxidation number (ON) decreased to between +2 and +3. The Mn_2O_3 species were reduced to a somewhat lesser extent in the CuMn-11/C catalyst (+2.24, frame F), while a higher extent of reduction took place in the CuMn-33/C catalyst (+2.03, frame E). The same Mn ON was obtained for the Cu-free MnO_x/C catalyst (+2.05) after a prolonged exposure at 543 K (frame B). The Cu and Mn oxidation states were confirmed by a more in-depth study using multivariate analysis in which no prior information on the component spectra was imposed and which yielded eigenspectra that corresponded well to the macrocrystalline Cu and Mn references with only a minor variation in the white line intensities (Figures S12–S13). Hence, we demonstrated for the first time that closely interacting Cu catalyzed the Mn_2O_3 reduction at much lower temperatures and determined the real Mn oxidation state in reduced $CuMnO_x$/C catalysts using time-resolved, *in situ* XAS.

for 2 h at 543 K (frame B), in agreement with the *ex situ* H_2 profiling (frame A). On the contrary, Mn_2O_3 in the $CuMnO_x$/C

ChemCatChem

Research Article
doi.org/10.1002/cctc.202200451

Chemistry
Europe
European Chemical
Societies Publishing

Impact of MnOx on the Catalyst Activity and Selectivity

The catalytic performance of the Cu catalysts in CO_2 and CO hydrogenation was influenced by the presence of MnO_x. Figure 4 shows a typical measurement in an H_2/CO_2 feed (frame A) and consecutively in an H_2/CO feed (frame B) at 40 bar pressure and different reaction temperatures (for a complete overview see Figure S5, frame A). All catalysts lost activity during the first 22 h on stream at 533 K (frame A) after which the conversion was relatively stable, especially at lower temperatures (473–513 K). The initial change in activity is ascribed to rearrangement of the Cu and promoter species.[53–56] When returning to the same reaction conditions after 92 h of catalysis only a slight additional loss of activity was observed, *e.g.* from 16.1% to 15.5% for the CuMn-11/C catalyst (indicated by the arrows in frame A). This means that, although carbon supports are known to have a relatively weak interaction with metal nanoparticles,[36] these catalysts are remarkably stable. In all cases we worked at conversion levels well below the thermodynamic equilibrium (*e.g.* 22.1% at 533 K in the H_2/CO_2 feed, Figures S5–S6) to study the intrinsic catalytic properties of these materials. The non- promoted Cu/C catalyst showed a considerable particle growth to at least *ca.* 12 nm, which was also observed in similar hydrogenation reactions,[37] while the Cu particle size was stable in $CuMnO_x/C$ catalysts (*e.g.* from 5.8 ± 1.6 to 6.3 ± 1.8 nm for the CuMn-5/C catalyst) (see also Table 1 and Figure S1). In other words, it is the MnO_x promoter that induces the unexpectedly high stability in these carbon-supported catalysts by suppressing the Cu particle growth.

Figure 5 (frame A) shows the CO_2 conversion of selected catalysts as a function of temperature, based on the same Cu mass (3.2 mg) for each catalyst. The Cu/C reference catalyst showed a CO_2 conversion up to 12.2% at 533 K, while the MnO_x/C reference sample did not show any significant CO_2 conversion. Combining MnO_x species and Cu nanoparticles only slightly increased the CO_2 conversion for intermediate MnO_x contents compared to the non-promoted Cu/C catalyst. The CuMn-11/C catalyst had a conversion of 15.2% at 533 K and considering the fresh average CuO_x particle size (Table 1) it has an estimated turnover frequency (TOF) of $6.4\pm2.2\cdot10^{-3}\,s^{-1}$,
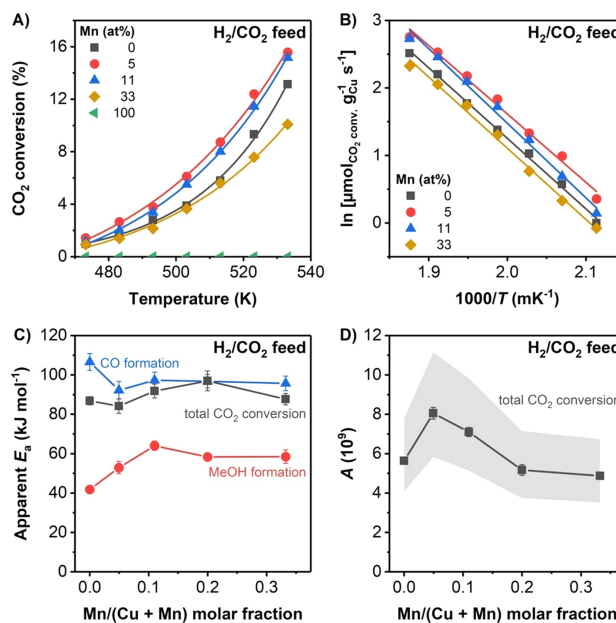
Figure 5. (**A**) CO_2 conversion as a function of temperature for selected $CuMnO_x/C$ catalysts determined from the activity after *ca.* 15 h at each temperature, neglecting the initiation period at 533 K. The data are fitted by an exponential curve. (**B**) Arrhenius plots based on the total amount of converted CO_2 using linear fits without restrictions. (**C**) Apparent activation energy as a function of the Mn content, determined for the total CO_2 conversion, MeOH formation, and CO formation. (**D**) Pre-exponential factor as a function of the Mn content based on the total CO_2 conversion using a fixed activation energy of 88.1 ± 1.4 kJ mol^{-1}. The error bars represent the error in the determination of the pre-exponential factor, while the shaded area indicates the width induced by the error in the fixed activation energy. Conditions: 40 bar(g), 690 mL min^{-1} g$_{Cu}^{-1}$, *ca.* 1,800 h^{-1}, 3.2 mg Cu, H_2/CO_2/He = 67.5/22.5/10 vol%.

which is in the same order of magnitude as for the Cu/C catalyst ($7.5\pm2.5\cdot10^{-3}\,s^{-1}$) (Figure S8). At all measured temperatures, an MnO_x content of 5–11 at% was sufficient to optimize the total activity, while at higher MnO_x loadings the conversion decreased. Frame B shows the Arrhenius plots of the selected catalysts (assuming zero-order kinetics, which is reasonable at the low conversion levels), which are translated in frame C to the apparent activation energy E_a as a function of the Mn content. The E_a to convert CO_2 appears to be independent of the Mn content and has an average value of 88.1 ± 1.4 kJ mol^{-1}, suggesting that in each of these catalysts the active site for CO_2 conversion is the same. For each promoted catalyst, the E_a for CO formation (95.7 ± 1.9 kJ mol^{-1}) is higher than the E_a for methanol formation (59.0 ± 1.2 kJ mol^{-1}). Frame D presents the apparent pre-exponential factor A as a function of the Mn loading using the average E_a for CO_2 conversion as a fixed value. The CuMn-5/C and CuMn-11/C catalysts have a slightly larger A, describing a higher probability of catalytic turnover and/or a higher density of active sites, and is in agreement with the higher total activity of these catalysts. However, the impact of MnO_x on the Cu activity in CO_2 conversion is minor.

The performance of the $CuMnO_x/C$ catalysts was also evaluated for the hydrogenation of CO, consecutive to the CO_2 hydrogenation experiment. Figure 6 (frame A) shows the CO
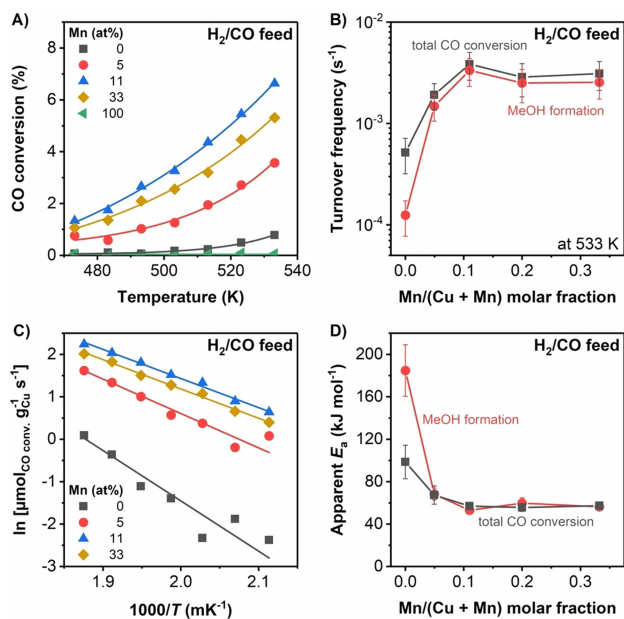
Figure 4. (**A**) CO_2 and (**B**) CO conversion as a function of time for selected $CuMnO_x/C$ catalysts, measured in a single test. The numbers in the top banners represent the reaction temperatures in K. Conditions: 40 bar(g), 690 mL min^{-1} g$_{Cu}^{-1}$, *ca.* 1,800 h^{-1}, 3.2 mg Cu, H_2/CO_2/He = 67.5/22.5/10 vol% or H_2/CO/He = 60/30/10 vol%.

ChemCatChem

Research Article
doi.org/10.1002/cctc.202200451

Chemistry
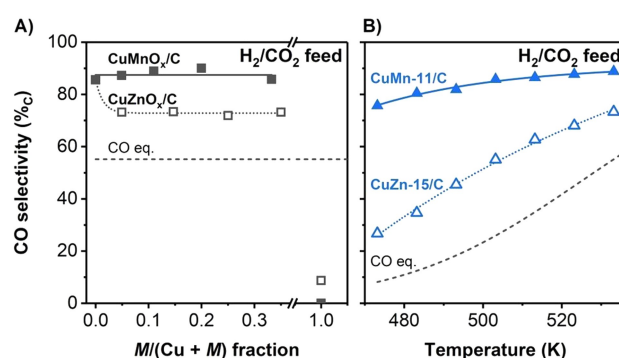**Europe**
European Chemical
Societies Publishing

Figure 6. (A) CO conversion as a function of temperature for selected CuMnO$_x$/C catalysts determined from the activity after *ca.* 15 h at each temperature, neglecting the initiation period at 533 K. The data are fitted by an increasing exponential curve. (B) Turnover frequency as a function of the Mn content determined at 533 K using surface-averaged particle size of the used catalysts. (C) Arrhenius plots using linear fits without restrictions. (D) Apparent activation energy as a function of the Mn content, determined for the total CO conversion and MeOH formation. Conditions: 40 bar(g), 690 mL min^{-1} g$_{Cu}$$^{-1}$, *ca.* 1,800 h^{-1}, 3.2 mg Cu, H$_2$/CO/He = 60/30/10 vol%.
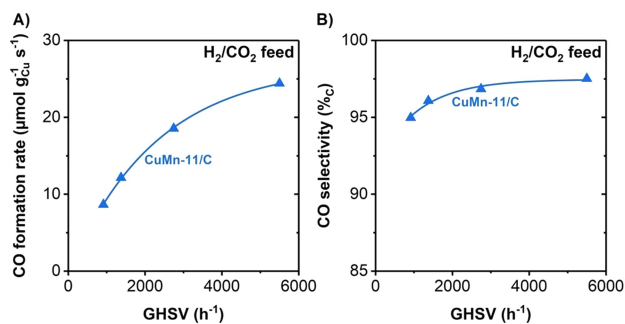
CO$_2$ hydrogenation over supported Cu nanoparticles can lead to the formation of either CO or methanol.[57,58] For example, at 533 K and 40 bar in our H$_2$/CO$_2$ feed the thermodynamically expected selectivity to CO is 55.2%$_C$ at an equilibrium CO$_2$ conversion of 22.1% (Figure S6). Figure 7 (frame A) shows the selectivity to CO in CO$_2$ hydrogenation at 533 K as a function of the MnO$_x$ content (filled symbols), while Figure S9 shows the selectivity to MeOH in an H$_2$/CO feed. For comparison, the same experiments were performed with a CuZnO$_x$/C catalyst series with similar metal loadings[37] and are included in the frame (hollow symbols). In an H$_2$/CO$_2$ feed, the major product was CO (> 72%$_C$) for all catalysts, which was formed by the reverse water-gas shift (RWGS) reaction in concentrations much higher than the equilibrium concentration (dashed line in frame A). Remarkably, MnO$_x$ promotion maintained the high CO selectivity of 86%$_C$, while ZnO$_x$ addition led to a lower CO selectivity (73%$_C$).

Figure 7 (frame B) shows the selectivity to CO in an H$_2$/CO$_2$ feed at 533 K as a function of temperature and comparing Mn and Zn promotion at similar promoter content. For both catalysts more CO is produced at increasing temperatures, as expected for the endothermic RWGS reaction (Eq. (2)). Interestingly, at all tested temperatures the CuMn-11/C catalyst was much more selective to CO than the CuZn-15/C catalyst, especially at low temperatures (*e.g.* 3 times more selective, at 470 K). This makes the CuMn-11/C catalyst an effective low-temperature RWGS catalyst. In the next section we further explore this remarkable difference between MnO$_x$ and ZnO$_x$ promotion of Cu-based catalysts in hydrogenation reactions.

Reaction conditions such as temperature, pressure, and gas flow per catalyst volume are key to tune the catalyst performance, specifically for CO$_2$ hydrogenation.[59] Figure 8 shows for the CuMn-11/C catalyst and at 20 bar pressure, the effect of the gas flow expressed as gas hourly space velocity (GHSV) on the Cu mass-normalized CO formation rate (frame A) and the CO selectivity (frame B). The CO formation rate increased from 8.7

conversion as a function of the reaction temperature for selected catalysts. Please note the smaller scale on the ordinate compared to Figure 5 (frame A). The MnO$_x$/C and Cu/C catalysts showed a very limited activity, but the CO conversion was greatly enhanced by the addition of MnO$_x$ to supported Cu nanoparticles. In our series, the MnO$_x$ content of 11 at% showed the highest total activity at each tested reaction temperature. As an example, at 533 K the CO conversion increased from 0.8% for the Cu/C catalyst to 6.6% for the CuMn-11/C catalyst. When taking the surface-averaged Cu(Mn)O$_x$ particle size of the used catalysts into account (Table 1), the MnO$_x$ promotion led to a total TOF enhancement of an order of magnitude as shown in frame B. This promotional effect is even more pronounced when focusing on the methanol formation (0.12 ± 0.05 to 3.3 ± 1.0·10^{-3} s^{-1}). In fact, upon promotion at least the same amount of by-products was formed in the CO/H$_2$ feed as for bare Cu catalysts, but additionally a large amount of methanol was formed, pointing to a high methanol selectivity for the newly formed Cu-promoter interface active sites. Using Arrhenius plots of the CuMnO$_x$/C catalysts in the H$_2$/CO feed (frame C), the apparent activation energy E_a for the total CO conversion (frame D) was determined. The large activity increase upon MnO$_x$ promotion is explained by a *ca.* 1.7 times decrease in the E_a from 99 ± 16 to 57.3 ± 1.3 kJ mol^{-1}. Our results clearly show that MnO$_x$ acts as a very efficient activity promoter for supported Cu nanoparticles in CO hydrogenation, while having little effect in an H$_2$/CO$_2$ feed.

Figure 7. Selectivity to CO during CO$_2$ hydrogenation, as a function of (A) MnO$_x$ or ZnO$_x$ loading at 533 K (M = Mn or Zn metal) and (B) reaction temperature (CO$_2$ conversion = 1.1–15.1% and 4.8–20.2% for CuMn-11/C and CuZn-15/C catalysts, respectively). The selectivity was determined after 15 h at each reaction condition. The dashed lines refer to the expected carbon-based CO selectivity at thermodynamic equilibrium, *e.g.* at 533 K the equilibrium composition is H$_2$/CO/CO$_2$/H$_2$O/H$_2$/He = 61.1/2.9/18.4/5.2/2.3/10 vol%. Conditions: 40 bar(g), 690 mL min^{-1} g$_{Cu}$$^{-1}$, *ca.* 1,800 h^{-1}, 3.2 mg Cu, H$_2$/CO$_2$/He = 67.5/22.5/10 vol%.

ChemCatChem

Research Article
doi.org/10.1002/cctc.202200451

Chemistry Europe
European Chemical
Societies Publishing

Figure 8. (A) CO formation rate and (B) CO selectivity as a function of gas hourly space velocity (GHSV) for the CuMn-11/C catalyst. The CO_2 conversion was between 7.8–17.4%. The only other product was methanol with traces of CH_4 ($< 0.3\%_C$). Conditions: 533 K, 20 bar(g), 1.1–6.4 mg Cu, $H_2/CO_2/He = 67.5/22.5/10$ vol%. Under these conditions the thermodynamic equilibrium concentration consists of $82.3\%_C$ CO. The data are fitted by an exponential curve.

to $24.4\ \mu mol\ g_{Cu}^{-1}\ s^{-1}$ for a higher gas flow per catalyst volume by a factor of 6. Also the CO selectivity slightly increased from $95\%_C$ to $98\%_C$ upon increasing the GHSV. These observations show that the methanol formation is suppressed at higher flow rates by promoting the desorption of adsorbed CO from the catalyst surface. Hence, supported $CuMnO_x$ is an effective RWGS catalyst at low temperature and high GHSV.

Comparison between MnO_x and ZnO_x Promotion

An interesting question is whether the MnO_x promoter acts in a similar manner as the well-established ZnO_x promoter for methanol synthesis. Figure 9 presents the catalytic performance of selected promoted Cu-based catalysts at 20 bar for the hydrogenation of either CO_2, CO, or a combination to methanol, mimicking the conditions during the *operando* XAS experiments. For a complete overview see Figure S5 (frame B). The activity of the CuMn-11/C catalyst is directly compared to a $CuZnO_x/C$ reference catalyst with a $Zn/(Cu+Zn)$ molar fraction of 0.15 and similar Cu particle size.[37] All catalysts stabilized
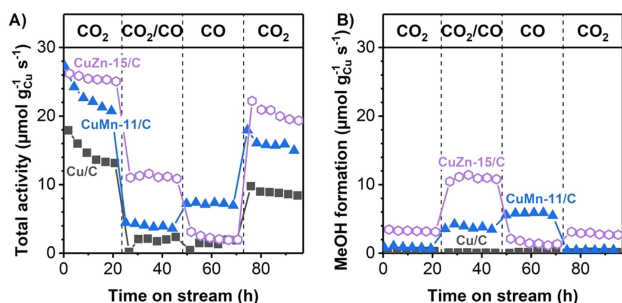
Figure 9. (A) Total activity in terms of converted CO_2 and/or CO and (B) methanol formation rate as a function of time on stream for the Cu/C and CuMn-11/C catalysts as well as for a reference CuZn-15/C catalyst. Conditions: 533 K, 20 bar, 1.0 L min^{-1} g$_{Cu}^{-1}$, *ca.* 2700 h^{-1}, 2.1 mg Cu, feeds: $H_2/CO_2/He = 67.5/22.5/10$ vol%, $H_2/CO_2/CO/He = 60/3/27/10$ vol%, and $H_2/CO/He = 60/30/10$ vol%.

within the first 22 h in a pure H_2/CO_2 feed (frame A), during which redistribution of the catalyst components is likely to occur.[53–56] Only a slight additional loss of activity was observed when returning to the same reaction conditions after 74 h of catalysis. The further decrease in activity of the catalysts, expressed as decrease % in CO_2 conversion, was limited to 13% for the CuZn-15/C and 16% for the CuMn-11/C catalysts.

The ZnO_x promoter behaved as expected from literature in the various feed compositions:[10,16,60] frame A shows a higher activity for the CuZn-based catalyst in H_2/CO_2 than in H_2/CO, mainly due to an increased RWGS reaction activity leading to *ca.* $87\%_C$ CO, while frame B shows that the highest methanol formation was observed when a small amount of CO_2 was added to the syngas feed.
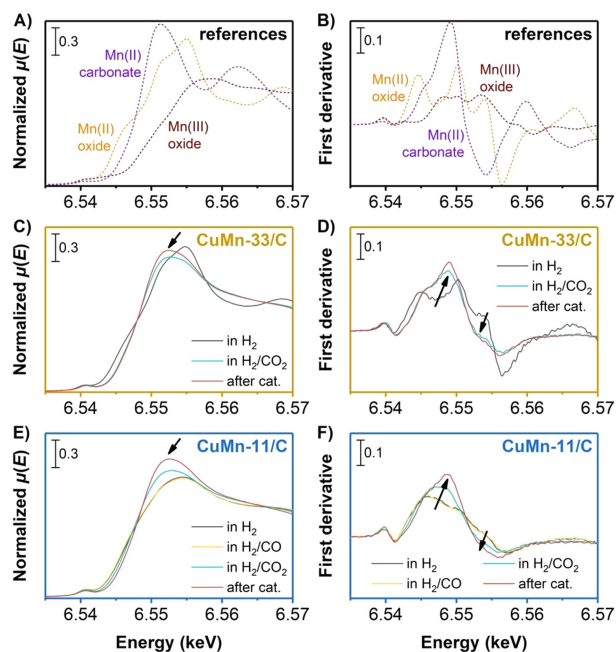
The behavior of the MnO_x promoter is quite different: the 3 vol% CO_2 in H_2/CO gave a low total activity (frame A) and methanol formation rate (frame B) for the CuMn-11/C catalyst. Another striking difference is that in the absence of CO_2 in the feed, MnO_x promotion is much more effective than ZnO_x promotion. Specifically, the total activity and the selectivity to methanol (80 *vs* $68\%_C$), and hence the methanol formation (5.8 *vs* $1.3\ \mu mol\ g_{Cu}^{-1}\ s^{-1}$), were *ca.* 4.5 times higher for MnO_x promotion than for the ZnO_x-promoted catalyst. A third major difference is that in an H_2/CO_2 feed the MnO_x promotion suppressed methanol formation and led to a high CO selectivity ($96\%_C$). These observations were irrespective of the promoter concentration (Figure S5, frame B). These results suggest that the interaction of CO_2 with the MnO_x promoter is fundamentally different than with the ZnO_x promoter.

MnO_x Speciation Studied with Operando Spectroscopy

The oxidation state and local surroundings of Cu and Mn species and the evolution of the MnO_x structure were studied by XAS experiments under working conditions (also termed *operando*) of 20 bar and 533 K at the ROCK beamline of SOLEIL, simultaneously at the Cu and Mn K-edges. Figure 10 shows a selection of normalized X-ray absorption spectra and corresponding first derivatives in the X-ray absorption near-edge structure (XANES) energy region. The spectra of several MnO_x references are shown in frames A–B. Spectra for the CuMn-33/C and CuMn-11/C catalysts in an H_2 atmosphere and during subsequent CO and CO_2 hydrogenation are given in frames C–F. An overview of all XAS spectra at the Cu and Mn K-edges is shown in Figures S14–S15. The speciation of the reduced Cu in the $CuMnO_x/C$ catalysts (Figure 3) did not change during catalysis, not even in the more oxidizing gas feed of H_2/CO_2, in line with literature on $CuZnO_x$ catalysts.[41,61] The result was confirmed by a more in-depth multivariate analysis (Figure S17).

Focusing on the promoter, the MnO_x in the CuMn-33/C catalyst (frame C) consisted of almost exclusively Mn(II)—O with an Mn ON of $+2.03$ after the *in situ* H_2 treatment. During 3.5 h of high-pressure CO_2 hydrogenation the white line of MnO at 6554.7 eV shifted to a lower energy by 2.2 eV (as indicated by the arrow) and after catalysis resembled the $MnCO_3$ reference. This reference is typical for Mn(II) strongly coordinated to a

ChemCatChem

Research Article
doi.org/10.1002/cctc.202200451

Chemistry Europe
European Chemical
Societies Publishing

Figure 10. (A) Reference (Mn_2O_3, MnO, and $MnCO_3$) XANES spectra and (B) corresponding first derivatives on the Mn K-edge at 298 K. (C–F) *Operando* XANES spectra and corresponding first derivatives on the Mn K-edge of the (C–D) CuMn-33/C and (E–F) CuMn-11/C catalysts. Depicted (1) in an H_2 atmosphere at 453 K after a treatment in 20 vol% H_2/He up to 543 K in 1 bar for *ca.* 25 min, (2) during subsequent H_2/CO and H_2/CO_2 conversion at 20 bar and 533 K after 160–210 min, and (3) after catalysis in H_2/CO_2 at 20 bar and 298 K. Gas compositions: H_2/CO/He = 60/30/10 vol% and H_2/CO_2/He = 67.5/22.5/10 vol%. The arrows indicate the formation of Mn(II) coordinated to a carbonated species upon H_2/CO_2 conversion.

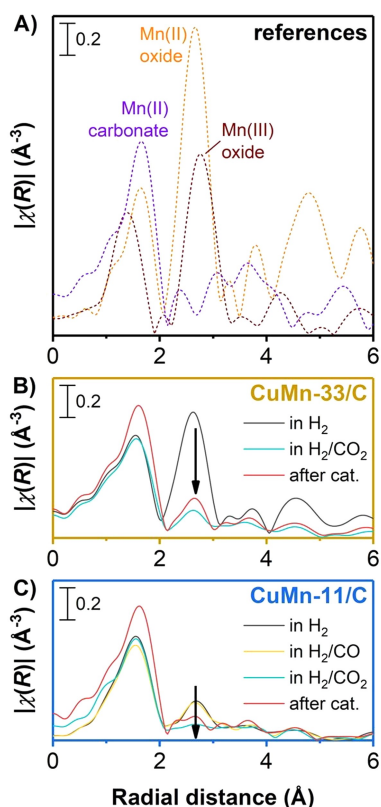carbonate species, or in other words *via* an oxygen bond to CO_2 (*i.e.* Mn(II)—O—CO_2). This spectral shift was already observed during pressurization to 20 bar in H_2/CO_2 at 453 K in *ca.* 2 h (Figure S16), conditions that are well below typical methanol synthesis reaction temperatures and pressures.[7,62] To verify the formation of an Mn(II)—O—CO_2-like compound we cooled the CuMn-33/C catalyst to room temperature in H_2/CO_2 (denoted as "after cat.") to obtain a higher resolution spectrum, still resembling that of the $MnCO_3$ reference. Please note that after catalysis no crystalline $MnCO_3$ was observed in the XRD patterns of the $CuMnO_x$/C catalysts (Figure S3, frame B). The average Mn ON did not further change during catalysis (*ca.* +2.04 at room temperature in a 20 bar H_2/CO_2 feed, see also Table S4), in line with a conversion of Mn(II)—O to Mn(II)—O—CO_2. The two isosbestic points at 6548 and 6558 eV provide a strong indication that Mn(II)—O binds CO_2 to form only one other species.[63] Also in the first derivative plot of the normalized absorption (frame D) the resemblance of the catalyst spectra in an H_2/CO_2 feed and the $MnCO_3$ reference is clear (as indicated by the arrows). Hence, *operando* XAS in an H_2/CO_2 feed strongly suggests the formation of Mn(II) strongly bound to a carbonate species because of the CO_2 interaction with Mn(II)—O.

The influence of the gas composition on the MnO_x speciation is studied in more detail for the CuMn-11/C catalyst (frames E–F). After the *in situ* reduction, we started with a mixed

MnO_x phase with an average Mn ON of +2.24 (see also Figure 3), which is in-between the MnO (Mn(II)) and Mn_2O_3 (Mn(III)) references. The spectral features of the CuMn-11/C did not change during more than 2.5 h of H_2/CO conversion. Even subsequent enrichment of the syngas feed with 3 vol% CO_2, which had a large influence on the promoter in the case of ZnO_x-promoted methanol synthesis,[6,8–10] did not influence the shape of the spectra (Figure S15). Yet, with the switch to an H_2/CO_2 feed, an Mn(II)—O—CO_2 complex was formed (frames E–F). These observations are supported by multivariate analysis on the Mn K-edge of the CuMn-11/C catalyst during subsequent changes in feed gas composition (Figure S18). In particular, the Mn speciation remained constant until the introduction of the H_2/CO_2 feed, after which a fingerprint of an Mn(II) carbonate-like compound was observed and became dominant after *ca.* 3 h. The formation of an Mn(II)—O—CO_2 complex during catalysis (Figure 9) indicates a strong CO_2 adsorption on the Mn promoter while locally few adsorbed H atoms are present, which may explain the lower total activity and methanol selectivity of the $CuMnO_x$/C catalysts when CO_2 is present in the feed. Therefore, during working conditions CO_2 has a strong impact on the local surroundings of the Mn species in $CuMnO_x$/C catalysts, thereby influencing the MnO_x promotion.

To differentiate between Mn(II)—O strongly binding CO_2 and crystalline $MnCO_3$ formation, it is important to consider the local coordination of the Mn atoms in the MnO_x promoter during high-pressure CO_2 and CO hydrogenation by carefully inspecting the extended X-ray absorption fine structure (EXAFS) energy region. Figure 11 shows the Fourier-transformed EXAFS region of macrocrystalline Mn references in standard conditions (frame A) and the CuMn-33/C (frame B) and CuMn-11/C (frame C) catalysts in the reduced state, during working conditions in an H_2/CO_2 feed, and after catalysis. The coordination numbers (CNs) and bond lengths from the EXAFS data analysis are summarized in Tables S5–S9. After the *in situ* reduction two significant signals were observed in both catalysts: the first-shell Mn—O bond at $R = 1.55$ Å and next an Mn—Mn bond at $R = 2.65$ Å, both resembling the MnO reference. In the CuMn-11/C catalyst the signal corresponding to the Mn—Mn bond is less intense than for the CuMn-33/C catalyst and significantly lower than for the Mn—Mn bond of the Mn_2O_3 reference. This result indicates a short-range ordering of the MnO_x promoter in the CuMn-11/C catalyst, in line with the theoretical partial coverage of MnO_x over the Cu^0 surface in this catalyst (73%).

The local environment of the MnO_x promoter did not change upon high-pressure conversion of H_2/CO. Also enriching the syngas feed with 3 vol% CO_2 for 4 h did not change the state of the MnO_x promoter, but that might be due to the slow CO_2 introduction at 20 bar. Only when CO_2 was hydrogenated, the spectra for both catalysts (Figure 11) significantly changed: the signal at $R = 2.65$ Å corresponding to the second-shell Mn—Mn bond of MnO_x decreased, and therefore resembled the Mn(II) carbonate reference. Interestingly, for the CuMn-33/C catalyst a fraction of the MnO phase remained present after catalysis, whereas for the CuMn-11/C catalyst the second-shell Mn—Mn bond peak completely vanished. The decrease in this

ChemCatChem

Research Article
doi.org/10.1002/cctc.202200451

Chemistry Europe
European Chemical
Societies Publishing

Figure 11. Fourier-transformed EXAFS spectra at the Mn K-edge of (**A**) macrocrystalline references (Mn_2O_3, MnO, and $MnCO_3$) at 298 K, (**B**) CuMn-33/C and (**C**) CuMn-11/C catalysts. The spectra of the catalysts are depicted (1) in an H_2 atmosphere at 453 K after *in situ* reduction (for exact conditions, see Figure 10) and (2) during high-pressure H_2/CO and subsequent H_2/CO_2 conversion at 533 K (for exact conditions, see Figure 10).

scattering path intensity is unlikely to be related to redispersion of the MnO_x phase over the carbon support,[46] as EDX maps of the CuMn-15/C catalyst confirm the presence of MnO_x phases in close proximity with the Cu nanoparticles (Figure 2, frame E). Hence, the decrease in the Mn–Mn scattering path intensity upon introducing an H_2/CO_2 feed can be attributed to the formation of an Mn(II)–O–CO_2-like compound and/or amorphization of the MnO_x phase, which is supported by the XRD analysis of the used CuMnOx/C catalysts in which no crystalline MnO_x phases were observed (Figure S3, frame B). Using *operando* XAS at simultaneously the Cu and Mn K-edges we unequivocally showed that the MnO_x promoter is predominantly in the MnO phase after *in situ* reduction and high-pressure CO hydrogenation, whereas during CO_2 hydrogenation the promoter speciation changes drastically and an Mn(II)–O–CO_2-like compound is formed.

Discussion

We observed a strong change in the MnO_x speciation in an H_2/CO_2 feed with *operando* XAS, while such effects were absent for ZnO_x in oxide-supported $CuZnO_x$ catalysts.[64–66] We investigated

the thermodynamic properties of the formation of $MnCO_3$ (as a representation for the Mn(II)–O–CO_2 complex) and $ZnCO_3$ in high-temperature CO_2 hydrogenation[67] to understand the different behavior of the MnO_x and ZnO_x promoters. Equations (3) and (4) show the thermodynamic parameters for the reactions of MnO and ZnO with CO_2 at 533 K and 1 bar (for more details see Table S9). Interestingly, under these conditions the formation of $MnCO_3$ is favored (negative $\Delta_r G$), whereas ZnO cannot spontaneously react with CO_2 to form $ZnCO_3$ (positive $\Delta_r G$). Even though the negative entropy ($\Delta_r S$) shows that the Gibbs free energy becomes more negative at higher pressure (*e.g.* 20 bar), CO_2 significantly binds stronger to MnO than to ZnO.

	$\Delta_r H_{533K}$ (kJ mol⁻¹)	$\Delta_r S_{533K}$ (J mol⁻¹ K⁻¹)	$\Delta_r G_{533K}$ (kJ mol⁻¹)	
$MnO_{(s)} + CO_{2(g)} \rightleftharpoons MnCO_{3(s)}$	−101	−164	−13.6	(3)
$ZnO_{(s)} + CO_{2(g)} \rightleftharpoons ZnCO_{3(s)}$	−68.7	−169	+21.6	(4)

The binding of CO_2 to MnO can represent various structures (Figure 12). For example, it can indicate strongly adsorbed CO_2 on the manganese and oxygen atoms of Mn(II)–O (structure A) or the closely related formation of crystalline $MnCO_3$ (structure B). For the first structure it implies that the Mn-(II)–O–CO_2-type complex only forms at the surface of the MnO_x promoter and hence lacks long-range crystallinity, while for the second structure the diffusion of CO_2 into the MnO is required. During catalysis we observed that the methanol productivity is influenced in a reversible manner by changing between CO_2-rich gas and pure syngas feeds (Figure 9) and after catalysis no crystalline $MnCO_3$ was observed in the XRD patterns of the $CuMnO_x$/C catalysts (Figure S3, frame B), making the second structure unlikely. Also the low Mn CN of 3.9 ± 0.3 for the first-shell Mn–O bond in an H_2/CO_2 feed is in line with structure A, while it makes the formation of crystalline $MnCO_3$ (having a corresponding Mn–O CN of 6) highly unlikely. Alternatively, the Mn(II)–O–CO_2-like structure might be envisioned as an ad-sorbed, oxygen-bound formate (HCOO*) species, which is a reaction intermediate typically found in Cu-catalyzed CO_2 hydrogenation,[68] on an Mn^0 surface formed following an H atom spillover from the Cu^0 surface (structure C). According to the binary phase diagram up to 26 at% Mn^0 can dissolve into Cu^0 nanoparticles at 533 K, forming a CuMn solid solution in coexistence with Cu_5Mn and Cu_3Mn phases.[69] Yet, no metallic Mn was observed in the XANES (Figure 10) or EXAFS analysis (Figure 11), which would be needed to support the Mn^0–HCOO structure, thereby making the formation of formates on the MnO_x promoter surface also highly unlikely. Hence, the spectral
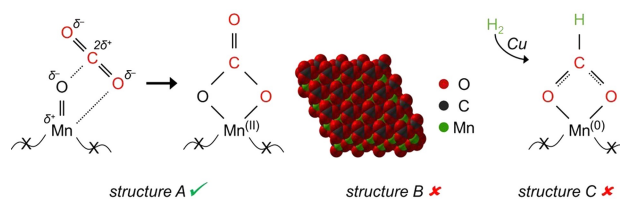

Figure 12. Theoretically possible structures for the Mn(II)–O–CO_2-type complex of which only structure A is supported by our data.

ChemCatChem

Research Article
doi.org/10.1002/cctc.202200451

Chemistry Europe
European Chemical
Societies Publishing

change upon H_2/CO_2 exposure is most probably related to the formation of strongly bound CO_2 to Mn(II)−O (structure A). More information about the exact nature of the complex could be obtained from DFT calculations on the stability of Mn(II)−O−CO_2-type complexes.

It must be noted that MnC_2 (amongst the Mn carbides) is a stable compound under the studied reaction conditions (Table S10), while Zn carbides are highly unstable. This suggests that MnC_2 might be (partially) formed during catalyst synthesis by the strong interaction between the graphite support and MnO in the presence of H_2 with concomitant H_2O formation. However, Figure 3 does not show any signal that can be attributed to MnC_2. Furthermore, the formation of MnC_2 from CO_2 under working conditions would require the scission of the C−O bond in the CO molecule, which is not expected to take place on Cu nanoparticles,[5,10,11] an MnO surface, or a Cu−MnO_x interface.

The first step in CO_2 hydrogenation is the adsorption of CO_2 on a catalyst surface (also termed CO_2*), which can either dissociate into O* and CO* directly or *via* a hydrogenated, carbon-bound carboxyl (HOCO*). The binding strength of the adsorbed CO on a Cu/oxide interface is a key factor for the product selectivity in CO_2 hydrogenation.[59] A weak CO* binding to the interface facilitates the desorption of CO* from the surface, while stronger bound CO* is likely to further hydrogenate to a carbon-bound formyl species (HCO*), one of the possible intermediates leading to the formation of methanol.[70] Figure 7 shows that the CO selectivity is not influenced upon MnO_x promotion of the supported Cu nanoparticles, while for the $CuZnO_x$/C catalysts the CO selectivity decreased from 86 to 73%$_C$ in favor of methanol. This can be explained by the weak interaction of CO* with Mn(II)−O or the Cu/MnO interface, while CO* has probably a stronger interaction with ZnO_x. Another important factor for the product selectivity is the surface coverage of adsorbed H atoms and CO_2, which both are needed to form either CO or methanol. To complete one turnover from CO_2 to CO requires only one H_2 molecule (*i.e.* two H* atoms) while three H_2 molecules are needed to produce one methanol molecule. The observed Mn(II)−O−CO_2 structure in the $CuMnO_x$/C catalysts by *operando* XAS (Figure 10) indicates a high CO_2* coverage on the MnO promoter, and hence a locally low H_2-to-CO_2 ratio. In this way, the relatively low H* surface concentration may suppress the hydrogenation of formyl species (HCO*), or the related oxygen-bound formate species (HCOO*),[68] to methanol and can explain the decrease in the methanol formation when CO_2 is added to the H_2/CO feed (Figure 9).

Figure 13 schematically depicts the proposed MnO_x speciation in $CuMnO_x$/C in an H_2 or H_2/CO feed (frame A) and in a high-pressure H_2/CO_2 feed (frame B). After *in situ* reduction by H_2 the average Mn ON of the MnO_x promoter is between +2.0 and +2.3 (Figure 3, frames E-F), and there is close contact between the Cu and Mn as evidenced by the reduction profile (Figure 3, frame A) and the EDX maps (Figure 2). These particles are in close proximity to Cu^0 nanoparticles as the reduction of Mn_2O_3 to MnO at intermediate temperatures is facilitated, as shown by *ex situ* H_2 profiling (Figure 3, frame A). The line scan
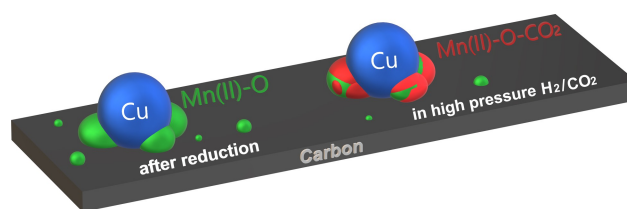
Figure 13. Schematic representation of the proposed MnO_x speciation in the $CuMnO_x$/C catalysts, depicted (**A**) after *in situ* reduction (and high-pressure CO hydrogenation) and (**B**) during CO_2 hydrogenation. Note that a limited amount of Cu_xMn alloys might be formed at each case.

in the EDX maps of the used catalyst (Figure 2, frames F-G) indicates that the Mn does not considerably cover the Cu surface or form an CuMn alloy but rather form separate MnO_x particles on the catalyst surface in close proximity to Cu. Upon CO_2 hydrogenation and subsequently after catalysis a significant amount of MnO is left in the CuMn-33/C catalyst but is almost completely absent in the CuMn-11/C catalyst (Figure 11, frames B–C). Mn(II)−O−CO_2 compounds probably only form at the MnO surface, as the diffusion of the required CO_2 into the MnO is limited.[71] This suggests for the CuMn-33/C catalyst converting H_2/CO_2, the formation of a layered Cu^0−MnO−Mn-(II)−O−CO_2 structure (from core to surface) and for the CuMn-11/C catalyst a complete transformation of the MnO_x to an Mn(II)−O−CO_2 compound.

Conclusions

Cu particles on graphitic carbon were prepared to study the MnO_x promotion in the hydrogenation of either CO_2 or CO. In an H_2/CO feed a modest amount of MnO_x, in close interaction with Cu, was already sufficient to enhance the activity of Cu/C thereby producing mainly methanol, and was much more effective than a $CuZnO_x$/SiO_2 catalyst with a similar promoter content. In CO_2 hydrogenation MnO_x promotion also increased the total activity with a selectivity to CO up to 87%$_C$ while retaining this high selectivity irrespective of the Mn content, even at lower temperatures (473 K), making $CuMnO_x$/C a low-temperature reverse water-gas shift catalyst. From X-ray absorption spectroscopy studies at high temperature and pressure we can explain this by the reversible formation of an Mn(II)−O−CO_2 complex, which has not been observed for the ZnO_x promoter. This surface-specific Mn speciation may indicate a high coverage of adsorbed CO_2 on MnO_x, while the local H atom coverage is relatively low; essential to suppress subsequent hydrogenation to methanol and lead to the desorption of adsorbed CO. This gives a direct insight into the nature of MnO_x promotion in Cu-based syngas conversion and allows a more rational use of reducible oxides in catalyst design.

ChemCatChem

Research Article
doi.org/10.1002/cctc.202200451

Chemistry Europe
European Chemical
Societies Publishing

Experimental

Chemicals

Copper nitrate ($Cu(NO_3)_2 \cdot 3H_2O$, Acros Organics, 99%), manganese nitrate ($Mn(NO_3)_2 \cdot 4H_2O$, Acros Organics), high surface area graphite (XG Sciences, xGnP® graphene nanoplatelets, grade C-500 HP, Brunauer-Emmett-Teller (BET) surface area of 490 $m^2 g^{-1}$, total pore volume of 0.84 $mL\,g^{-1}$), and nitric acid (HNO_3, Merck, 65%) were used as received. As a reference we used a series of $CuZnO_x$ nanoparticles supported on graphitic carbon with varying Zn/Cu molar ratios but similar Cu particles sizes, as previously reported.[37] Silicon carbide (SiC, Alfa Aesar, $\geq$98.8%, 46 grit) was pressed and sieved in a 212–425 μm fraction, calcined at 1073 K for 10 h, subsequently washed with 65% HNO_3, rinsed with water until pH 7 was reached, and finally dried at 393 K overnight before use.

Catalyst Synthesis

A series of $CuMnO_x/C$ catalysts, with similar Cu weight loadings (8.4 wt%) but varying Mn/Cu molar ratios, were prepared *via* incipient wetness impregnation, according to a previously reported method.[46] Typically, *ca.* 2 g of high surface area graphite was dried at 443 K under dynamic vacuum for 1.5 h. After cooling to room temperature the fine carbon powder was (co-)impregnated to incipient wetness, which means that the added liquid corresponds to 95% of the total pore volume (0.84 $mL\,g^{-1}$) as measured by N_2 physisorption at a p/p_0 value of 0.995, under static vacuum with a 0.1 M HNO_3 aqueous solution of *ca.* 1.8 M copper nitrate and up to 0.9 M manganese nitrate. The impregnated support was equilibrated at room temperature under static vacuum for 2 h prior to drying under dynamic vacuum for 24 h. The dried material was transferred to an Ar-filled glovebox and subsequently divided over two plug-flow reactors (1 g each) without exposure to air. The dried precursor was decomposed at 503 K (ramp 0.5 $K\,min^{-1}$) in an N_2 flow of 100 $mL\,min^{-1}\,g^{-1}$ for 1 h. After cooling to 303 K the material was exposed to 10 vol% O_2/N_2 for 3 h and subsequently to pure N_2 for 30 min. Finally, the sample was reduced at 443 K (ramp 2 $K\,min^{-1}$) in a 100 $mL\,min^{-1}\,g^{-1}$ flow of 10 vol% H_2/N_2 for 2 h, directly followed at 673 K (ramp 2 $K\,min^{-1}$) for 1 h. A part of the reduced catalyst was stored in an Ar-filled glovebox, whereas the remainder was slowly passivated in air at room temperature. The obtained $CuMnO_x/C$ catalysts are named CuMn-*X*/C, in which *X* represents the molar Mn/(Cu + Mn) fraction in percentages. An MnO_x/C catalyst (7.2 wt% Mn) was prepared in a similar manner.

Catalyst Characterization

Structural Characterization. Catalysts were imaged by transmission electron microscopy (TEM) using a Thermo Fisher Scientific Talos L120 C apparatus, operating at 120 kV. The samples were prepared by loading finely ground, dry sample ($<$25 μm) onto holey carbon film-coated Cu grids (Agar, 300 mesh). At least 540 individual particles at various locations within the sample were measured to determine the number-averaged CuO_x particle sizes (d_N). Also surface-averaged sizes (d_S) were calculated using

$$d_S \pm s_S = \sqrt{\frac{1}{N}\sum_{i=1}^{N} d_i^2} \pm \sqrt{\frac{1}{N-1}\sum_{i=1}^{N}(d_i - d_S)^2}$$, in which s_S represents the width of the lognormal particle size distribution, d_i the diameter of the *i*-th particle, and *N* the total number of measured particles. Only the relevant part of the lognormal distribution ($>$1% of maximum) was considered for the calculation of the average particle sizes. High-resolution, energy-dispersive X-ray spectroscopy (EDX) data

were acquired using a Spectra 300 transmission electron microscope (Thermo Fischer Scientific) operated at 300 kV. The EDX maps were typically recorded at a magnification of 1.3 Mx and were 512 × 512 pixels in size (6.5 pixels/nm) using a dwell time of 10 μs per pixel. Each map is an average of *ca.* 550 frames acquired over a total measurement time of 30 min.

Powder X-ray diffractograms of the catalysts were recorded in the reduced state and after air exposure on a Bruker AXS D8 Advance diffractometer at room temperature with a variable divergence slit. Samples were exposed to Co Kα radiation (λ = 1.790 Å) at 30 kV and 45 mA. The Scherrer equation was used to calculate the CuO_x crystallite sizes from the peak widths, thereby taking the instrumental line broadening of the X-ray diffraction (XRD) apparatus (*ca.* 0.1°) into account. All diffractograms were normalized between 0 and 1, *i.e.* between the lowest intensity at 20° and the maximum peak intensity due to the *(002)* reflection of graphite at 30.9°.

Temperature-programmed reduction (TPR) by H_2 was performed on a Micromeritics AutoChem II 2920 apparatus. Prior to the reduction the samples (50 mg each, $<$75 μm granulites) were dried at 393 K under an Ar flow of 50 $mL\,min^{-1}$ for 30 min and cooled to room temperature. Reduction profiles were recorded with a thermal conductivity detector when the samples were exposed to a 5 vol% H_2/Ar flow of 25 $mL\,min^{-1}$ up to 973 K with a ramp of 2.5 $K\,min^{-1}$. H_2O was captured with a dry ice/isopropanol cold trap.

XAS Analysis. *Operando*, quick X-ray absorption spectroscopy measurements on quasi-simultaneously the Cu (8979 eV) and Mn K-edge (6540 eV) were performed at the SOLEIL synchrotron (ROCK beamline).[72] Typically, 2-4 mg CuMn-11/C, CuMn-33/C, or MnO_x/C catalyst (25–75 μm sieve fraction) was loaded in a quartz capillary (internal diameter 1.2 mm, 20–50 μm thick), which was tightly glued into a frame connected to gas feed lines. A hot gas blower (FMD Oxford) controlled heating of the capillary. After the capillary was leak-checked at 20 bar, XAS data was obtained in He at room temperature. The catalyst was exposed to a 10 $mL\,min^{>M->1}$ flow of 20 vol% H_2/He and heated to 543 K (ramp 2.5 $K\,min^{-1}$) at ambient pressure with a hold time of 20–30 min (or 130 min for the MnO_x/C catalyst).

After the H_2 treatment the capillary containing the CuMn-11/C catalyst was cooled to 453 K prior to introducing a syngas feed ($H_2/CO/He = 60/30/10$ vol%) at 10 $mL\,min^{-1}$. Within *ca.* 100 min the capillary was pressurized to 20 bar after which the temperature was increased to 533 K (ramp 2.5 $K\,min^{-1}$) and held for 160 min. The feed was switched to $H_2/CO/CO_2/He = 60/27/3/10$ vol%, recording spectra for at least 200 min, and similarly to $H_2/CO_2/He = 67.5/22.5/10$ vol%. The CuMn-33/C catalyst was only measured under the H_2/CO_2 atmosphere. Finally, spectra were recorded for both catalysts after cooling to room temperature under 20 bar of H_2/CO_2.

During all treatments XAS spectra were obtained in the rocking mode, switching from the Cu K-edge (8.70–9.86 keV, 50 scans, 35 s) to the Mn K-edge (6.40–7.10 keV, 60 scans, 40 s) using 10 s to switch between each edge. The setup was configured in the transmission mode using as Si(111) quick-XAS monochromator. The product gas compositions were recorded with a mass spectrometer (Cirrus, MKS) at ambient pressure. When flowing CO gas, a carbonyl trap was used upstream of the capillary reactor. MnO (Sigma Aldrich, 99%), $MnCO_3$ (abcr, 99.985%), Mn_2O_3 (Sigma Aldrich, 99%), MnO_2 (Sigma Aldrich, $\geq$99%), CuO (Sigma Aldrich, 99.999%), Cu_2O (Sigma Aldrich, $\geq$99.99%), all mixed with boron nitride (Sigma Aldrich, 98%), as well as Cu (6 μm) and Mn (4 μm) foils were used as references with the spectra being recorded at room temperature

ChemCatChem

Research Article
doi.org/10.1002/cctc.202200451

Chemistry Europe
European Chemical
Societies Publishing

under air. The XAS spectra were processed using the Demeter software package,[73] as described in more detail in the Supplementary Information (section S3).

Catalyst Testing

Catalysts were tested in a 16-reactor setup (Flowrence, Avantium) for at least 80 h, operating at 20–40 bar(g) and 473–533 K using various CO_2 and CO feeds. The catalyst powders were pelletized and sieved into granules with a size of 75 to 150 μm. The stainless steel reactors (internal diameter 2.6 mm) were loaded with similar amounts of catalysts (either *ca.* 26 or 39 mg) and diluted with 400–450 mg inert SiC (sieve fraction of 212–425 μm), resulting in SiC contents of *ca.* 83 vol% of the total packed bed.[74] The different sizes of the sieve fractions of the catalysts and the diluent facilitated separation after catalysis and hence post-analysis by EM and XRD.

Two separate catalytic tests were performed to evaluate the influence of various parameters, such as the gas composition, temperature, pressure, and flow rate, on the catalyst performance. Prior to both tests, the catalysts were *in situ* reduced in a 20 vol% H_2/N_2 flow at 10.9 mL min^{-1} and 543 K for 2 h after which the temperature was lowered to 393 K. During the first test (see Figure S5, frame A, for an overview as a function of time) the reduced catalysts were exposed to a 2.2 mL min^{-1} flow of $H_2/CO_2/$He = 67.5/22.5/10 vol% at 690 mL min^{-1} g$_{Cu}^{-1}$ and a gas-hourly space velocity (GHSV) of *ca.* 1,800 h^{-1}, after which the reactors were pressurized to 40 bar(g) and heated to 533 K at 5 K min^{-1}. After 22 h the temperature was lowered to 473 K and consecutively increased in steps of 10 K to 533 K, recording data for 15 h at each reaction condition. In the same test, this temperature protocol was directly repeated in a flow of $H_2/CO/$He = 60/30/10 vol% at 40 bar(g). In the second test (see Figure S5, frame B, for an overview as a function of time), freshly reduced catalysts were exposed to varying gas compositions ($H_2/CO_2/$He, $H_2/CO/CO_2/$He = 60/27/3/10 vol%, and $H_2/CO_2/$He) at a pressure of 20 bar, maintaining constant flow rate of 1.0 mL min^{-1} g$_{Cu}^{-1}$ at *ca.* 2700 h^{-1} and temperature of 533 K. In the same test, this specific protocol was directly repeated at a pressure of 40 bar. Catalytic tests were performed at 20 bar, to have a direct comparison to the operando XAS experiments for which higher than 20 bar was not possible, and at 40 bar, to be closer to industrially relevant pressures.

A tri-phase carbonyl trap (active carbon, γ-Al_2O_3, ZnO) was located between the CO feed and the reactor to remove metal carbonyls and sulfur species. Products were analyzed by online gas chromatography every 15 min. He, H_2, CO, CO_2 were analyzed and quantified using a thermal conductivity detector, while oxygenates (up to pentanol) and hydrocarbons (ranging from C1 to C11) were analyzed and quantified by two separate flame ionization detectors. After catalysis, the samples were slowly exposed to air at 338 K. Details on the calculations of activity and selectivity are given in the Supplementary Information (section S4).

Author contributions

RD, LB, and PdJ conceived the experiments. RD and LB synthesized the catalysts and measured their performance, NV designed the catalyst synthesis protocol and performed basic electron microscopy, and JvdH performed the high-resolution electron imaging experiments. RD, LB, and PdJ performed the XAS experiments together with XC and GT. LB analyzed the XAS data. FM helped with multivariate analysis. FM and AvdE helped

with the interpretation of XAS data. JS helped in discussing the results. PdJ and KdJ provided guidance in discussing the results and writing the manuscript. All authors contributed to the final manuscript.

Conflict of Interest

The authors declare no conflict of interest.

Data Availability Statement

The data that support the findings of this study are available from the corresponding author upon reasonable request.

[1] B. E. Koel, J. Kim, in *Handb. Heterog. Catal.*, Wiley-VCH Verlag GmbH & Co. KGaA, Weinheim, Germany, **2008**, pp. 1593–1624.

[2] D. A. King, D. P. Woodruff, Eds., *Coadsorption, Promoters and Poisons*, Elsevier, **1993**.

[3] M. D. Argyle, C. H. Bartholomew, *Catalysts* **2015**, *5*, 145–269.

[4] M. Behrens, F. Studt, I. Kasatkin, S. Kühl, M. Hävecker, F. Abild-Pedersen, S. Zander, F. Girgsdies, P. Kurr, B.-L. Kniep, M. Tovar, R. W. Fischer, J. K. Nørskov, R. Schlögl, *Science* **2012**, *336*, 893–897.

[5] R. van den Berg, G. Prieto, G. Korpershoek, L. I. van der Wal, A. J. van Bunningen, S. Lægsgaard-Jørgensen, P. E. de Jongh, K. P. de Jong, *Nat. Commun.* **2016**, *7*, 13057.

[6] R. Dalebout, N. L. Visser, C. E. L. Pompe, K. P. de Jong, P. E. de Jongh, *J. Catal.* **2020**, *392*, 150–158.

[7] K. C. Waugh, *Catal. Today* **1992**, *15*, 51–75.

[8] J. S. Lee, K. H. Lee, S. Y. Lee, Y. G. Kim, *J. Catal.* **1993**, *144*, 414–424.

[9] M. Sahibzada, I. S. Metcalfe, D. Chadwick, *J. Catal.* **1998**, *174*, 111–118.

[10] K. Klier, V. Chatikavanij, R. G. Herman, G. W. Simmons, *J. Catal.* **1982**, *74*, 343–360.

[11] M. B. Fichtl, D. Schlereth, N. Jacobsen, I. Kasatkin, J. Schumann, M. Behrens, R. Schlögl, O. Hinrichsen, *Appl. Catal. A* **2015**, *502*, 262–270.

[12] M. B. Fichtl, J. Schumann, I. Kasatkin, N. Jacobsen, M. Behrens, R. Schlögl, M. Muhler, O. Hinrichsen, *Angew. Chem. Int. Ed.* **2014**, *53*, 7043–7047; *Angew. Chem.* **2014**, *126*, 7163–7167.

[13] J. Graciani, K. Mudiyanselage, F. Xu, A. E. Baber, J. Evans, S. D. Senanayake, D. J. Stacchiola, P. Liu, J. Hrbek, J. F. Sanz, J. A. Rodriguez, *Science* **2014**, *345*, 546–550.

ChemCatChem

Research Article
doi.org/10.1002/cctc.202200451

Chemistry Europe
European Chemical
Societies Publishing

[14] S. Zander, E. L. Kunkes, M. E. Schuster, J. Schumann, G. Weinberg, D. Teschner, N. Jacobsen, R. Schlögl, M. Behrens, *Angew. Chem. Int. Ed.* **2013**, *52*, 6536–6540; *Angew. Chem.* **2013**, *125*, 6664–6669.

[15] O. Martin, A. J. Martín, C. Mondelli, S. Mitchell, T. F. Segawa, R. Hauert, C. Drouilly, D. Curulla-Ferré, J. Pérez-Ramírez, *Angew. Chem. Int. Ed.* **2016**, *55*, 6261–6265; *Angew. Chem.* **2016**, *128*, 6369–6373.

[16] F. Studt, M. Behrens, E. L. Kunkes, N. Thomas, S. Zander, A. Tarasov, J. Schumann, E. Frei, J. B. Varley, F. Abild-Pedersen, J. K. Nørskov, R. Schlögl, *ChemCatChem* **2015**, *7*, 1105–1111.

[17] F. M. Pinto, V. Y. Suzuki, R. C. Silva, F. A. La Porta, *Front. Mater.* **2019**, *6*, 260.

[18] A. Ruiz Puigdollers, P. Schlexer, S. Tosoni, G. Pacchioni, *ACS Catal.* **2017**, *7*, 6493–6513.

[19] S. Kattel, B. Yan, Y. Yang, J. G. Chen, P. Liu, *J. Am. Chem. Soc.* **2016**, *138*, 12440–12450.

[20] M. K. Koh, Y. J. Wong, S. P. Chai, A. R. Mohamed, *J. Ind. Eng. Chem.* **2018**, *62*, 156–165.

[21] Y. Qin, S. Fan, X. Li, G. Gan, L. Wang, Z. Yin, X. Guo, M. O. Tadé, S. Liu, *ACS Appl. Nano Mater.* **2021**, *4*, 11969–11979.

[22] G. Wang, D. Mao, X. Guo, J. Yu, *Int. J. Hydrogen Energy* **2019**, *44*, 4197–4207.

[23] J. Słoczyński, R. Grabowski, A. Kozłowska, P. Olszewski, M. Lachowska, J. Skrzypek, J. Stoch, *Appl. Catal. A* **2003**, *249*, 129–138.

[24] V. D. B. C. Dasireddy, N. S. Štefančič, M. Huš, B. Likozar, *Fuel* **2018**, *233*, 103–112.

[25] S. Kuld, M. Thorhauge, H. Falsig, C. F. Elkjaer, S. Helveg, I. Chorkendorff, J. Sehested, *Science* **2016**, *352*, 969–974.

[26] H. Zhan, F. Li, C. Xin, N. Zhao, F. Xiao, W. Wei, Y. Sun, *Catal. Lett.* **2015**, *145*, 1177–1185.

[27] H. Chen, J. Lin, K. Tan, J. Li, *Appl. Surf. Sci.* **1998**, *126*, 323–331.

[28] J. González-Arias, M. González-Castaño, M. Elena Sánchez, J. Cara-Jiménez, H. Arellano-García, *Renewable Energy* **2022**, *182*, 443–451.

[29] M. Acet, H. Zähres, W. Stamm, E. F. Wassermann, W. Pepperhoff, *Phys. B Phys. Condens. Matter* **1989**, *161*, 67–71.

[30] Y. Lang, C. Du, Y. Tang, Y. Chen, Y. Zhao, R. Chen, X. Liu, B. Shan, *Int. J. Hydrogen Energy* **2020**, *45*, 8629–8639.

[31] J.-L. Li, T. Takeguchi, T. Inui, *Appl. Catal. A* **1996**, *139*, 97–106.

[32] M. Kilo, J. J. Weigel, A. Wokaun, R. A. Koeppel, A. Stoeckli, A. Baiker, *J. Mol. Catal. A* **1997**, *126*, 169–184.

[33] J. S. Hayward, P. J. Smith, S. A. Kondrat, M. Bowker, G. J. Hutchings, *ChemCatChem* **2017**, *9*, 1655–1662.

[34] H. Blanco, S. H. Lima, V. de Oliveira Rodrigues, L. A. Palacio, A. da Costa Faro Jr., *Appl. Catal. A* **2019**, *579*, 65–74.

[35] W. R. A. M. Robinson, J. C. Mol, *Appl. Catal.* **1991**, *76*, 117–129.

[36] R. Chatterjee, S. Kuld, R. van den Berg, A. Chen, W. Shen, J. M. Christensen, A. D. Jensen, J. Sehested, *Top. Catal.* **2019**, *62*, 649–659.

[37] R. Dalebout, L. Barberis, G. Totarella, S. J. Turner, C. La Fontaine, F. M. F. de Groot, X. Carrier, A. M. J. van der Eerden, F. Meirer, P. E. de Jongh, *ACS Catal.* **2022**, *12*, 6628–6639.

[38] X. Shi, X. Lin, R. Luo, S. Wu, L. Li, Z.-J. Zhao, J. Gong, *JACS Au* **2021**, *1*, 2100–2120.

[39] G. R. Johnson, S. Werner, A. T. Bell, *ACS Catal.* **2015**, *5*, 5888–5903.

[40] M. Zabilskiy, V. L. Sushkevich, M. A. Newton, J. A. van Bokhoven, *ACS Catal.* **2020**, *10*, 14240–14244.

[41] M. Zabilskiy, V. L. Sushkevich, D. Palagin, M. A. Newton, F. Krumeich, J. A. van Bokhoven, *Nat. Commun.* **2020**, *11*, 2409.

[42] G. T. Whiting, F. Meirer, B. M. Weckhuysen, in *XAFS Tech. Catal. Nanomater. Surfaces* (Eds.: Y. Isawa, K. Asakura, M. Tada), Springer International Publishing, Switzerland, **2017**, pp. 167–191.

[43] F. Bonino, E. Groppo, C. Prestipino, G. Agostini, A. Piovano, D. Gianolio, L. Mino, E. Gallo, C. Lamberti, in *Synchrotron Radiat. Basics, Methods Appl.* (Eds.: S. Mobilio, F. Boscherini, C. Meneghini), Springer-Verlag, Berlin-Heidelberg, Germany, **2015**, pp. 717–736.

[44] S. Bordiga, E. Groppo, G. Agostini, J. A. van Bokhoven, C. Lamberti, *Chem. Rev.* **2013**, *113*, 1736–1850.

[45] G. Totarella, R. Beerthuis, N. Masoud, C. Louis, L. Delannoy, P. E. de Jongh, *J. Phys. Chem. C* **2021**, *125*, 366–375.

[46] R. Beerthuis, N. L. Visser, J. E. S. van der Hoeven, P. Ngene, J. M. S. Deeley, G. J. Sunley, K. P. de Jong, P. E. de Jongh, *J. Catal.* **2020**, 0–8.

[47] R. Beerthuis, J. W. de Rijk, J. M. S. Deeley, G. J. Sunley, K. P. de Jong, P. E. de Jongh, *J. Catal.* **2020**, *388*, 30–37.

[48] J. L. Figueiredo, *J. Mater. Chem. A* **2013**, *1*, 9351–9364.

[49] J. L. Figueiredo, M. F. R. Pereira, M. M. A. Freitas, J. J. M. Órfão, *Carbon* **1999**, *37*, 1379–1389.

[50] M. L. Smith, A. Campos, J. J. Spivey, *Catal. Today* **2012**, *182*, 60–66.

[51] G. Fierro, M. Lo Jacono, M. Inversi, P. Porta, F. Cioci, R. Lavecchia, *Appl. Catal. A* **1996**, *137*, 327–348.

[52] E. Kleymenov, J. Sa, J. Abu-Dahrieh, D. Rooney, J. A. van Bokhoven, E. Troussard, J. Szlachetko, O. Safonova, M. Nachtegaal, *Catal. Sci. Technol.* **2012**, *2*, 373–378.

[53] P. L. Hansen, J. B. Wagner, S. Helveg, J. R. Rostrup-Nielsen, B. S. Clausen, H. Topsøe, *Science* **2002**, *295*, 2053–2055.

[54] P. C. K. Vesborg, I. Chorkendorff, I. Knudsen, O. Balmes, J. Nerlov, A. M. Molenbroek, B. S. Clausen, S. Helveg, *J. Catal.* **2009**, *262*, 65–72.

[55] G. Prieto, J. Zečević, H. Friedrich, K. P. De Jong, P. E. De Jongh, *Nat. Mater.* **2013**, *12*, 34–39.

[56] C. Holse, C. F. Elkjær, A. Nierhoff, J. Sehested, I. Chorkendorff, S. Helveg, J. H. Nielsen, *J. Phys. Chem. C* **2015**, *119*, 2804–2812.

[57] A. Bansode, B. Tidona, P. R. von Rohr, A. Urakawa, *Catal. Sci. Technol.* **2013**, *3*, 767–778.

[58] M. D. Porosoff, B. Yan, J. G. Chen, *Energy Environ. Sci.* **2016**, *9*, 62–73.

[59] S. Kattel, P. Liu, J. G. Chen, *J. Am. Chem. Soc.* **2017**, *139*, 9739–9754.

[60] C. Wu, L. Lin, J. Liu, J. Zhang, F. Zhang, T. Zhou, N. Rui, S. Yao, Y. Deng, F. Yang, W. Xu, J. Luo, Y. Zhao, B. Yan, X.-D. Wen, J. A. Rodriguez, D. Ma, *Nat. Commun.* **2020**, *11*, 5767.

[61] R. Naumann d'Alnoncourt, X. Xia, J. Strunk, E. Löffler, O. Hinrichsen, M. Muhler, *Phys. Chem. Chem. Phys.* **2006**, *8*, 1525–1538.

[62] K. A. Almusaiteer, A. Al-Hadhrami, O. Abed, G. Biausque, A. Al-Amer, *Catalysts and Methods for Methanol Synthesis from Direct Hydrogenation of Syngas and/or Carbon Dioxide*, **2019**, US20190076828 A1.

[63] D. V. Stynes, *Inorg. Chem.* **1975**, *14*, 453–454.

[64] N. J. Divins, D. Kordus, J. Timoshenko, I. Sinev, I. Zegkinoglou, A. Bergmann, S. W. Chee, S. Widrinna, O. Karslıoğlu, H. Mistry, M. Lopez Luna, J. Q. Zhong, A. S. Hoffman, A. Boubnov, J. A. Boscoboinik, M. Heggen, R. E. Dunin-Borkowski, S. R. Bare, B. Roldan Cuenya, *Nat. Commun.* **2021**, *12*, 1435.

[65] D. Großmann, K. Klementiev, I. Sinev, W. Grünert, *ChemCatChem* **2017**, *9*, 365–372.

[66] M. W. E. Van Den Berg, S. Polarz, O. P. Tkachenko, K. Kähler, M. Muhler, W. Grünert, *Catal. Lett.* **2009**, *128*, 49–56.

[67] A. Roine, P. Lamberg, J. Mansikka-aho, P. Björklund, J.-P. Kentala, T. Talonen, T. Kotiranta, R. Ahlberg, A. Gröhn, O. Saarinen, J. Myyri, J. Sipilä, A. Vartiainen, *Metso Outotec HSC Chemistry v7.14 Software* **2011**, 7.14.

[68] L. C. Grabow, M. Mavrikakis, *ACS Catal.* **2011**, *1*, 365–384.

[69] H. Okamoto, *J. Phase Equilib. Diffus.* **2018**, *39*, 87–100.

[70] S. Kattel, B. Yan, Y. Yang, J. G. Chen, P. Liu, *J. Am. Chem. Soc.* **2016**, *138*, 12440–12450.

[71] P. Kofstad, *Solid State Ionics* **1984**, *12*, 101–111.

[72] C. La Fontaine, S. Belin, L. Barthe, O. Roudenko, V. Briois, *Synchrotron Radiat. News* **2020**, *33*, 20–25.

[73] B. Ravel, M. Newville, *J. Synchrotron Radiat.* **2005**, *12*, 537–541.

[74] C. M. van den Bleek, K. van der Wiele, P. J. van den Berg, *Chem. Eng. Sci.* **1969**, *24*, 681–694.